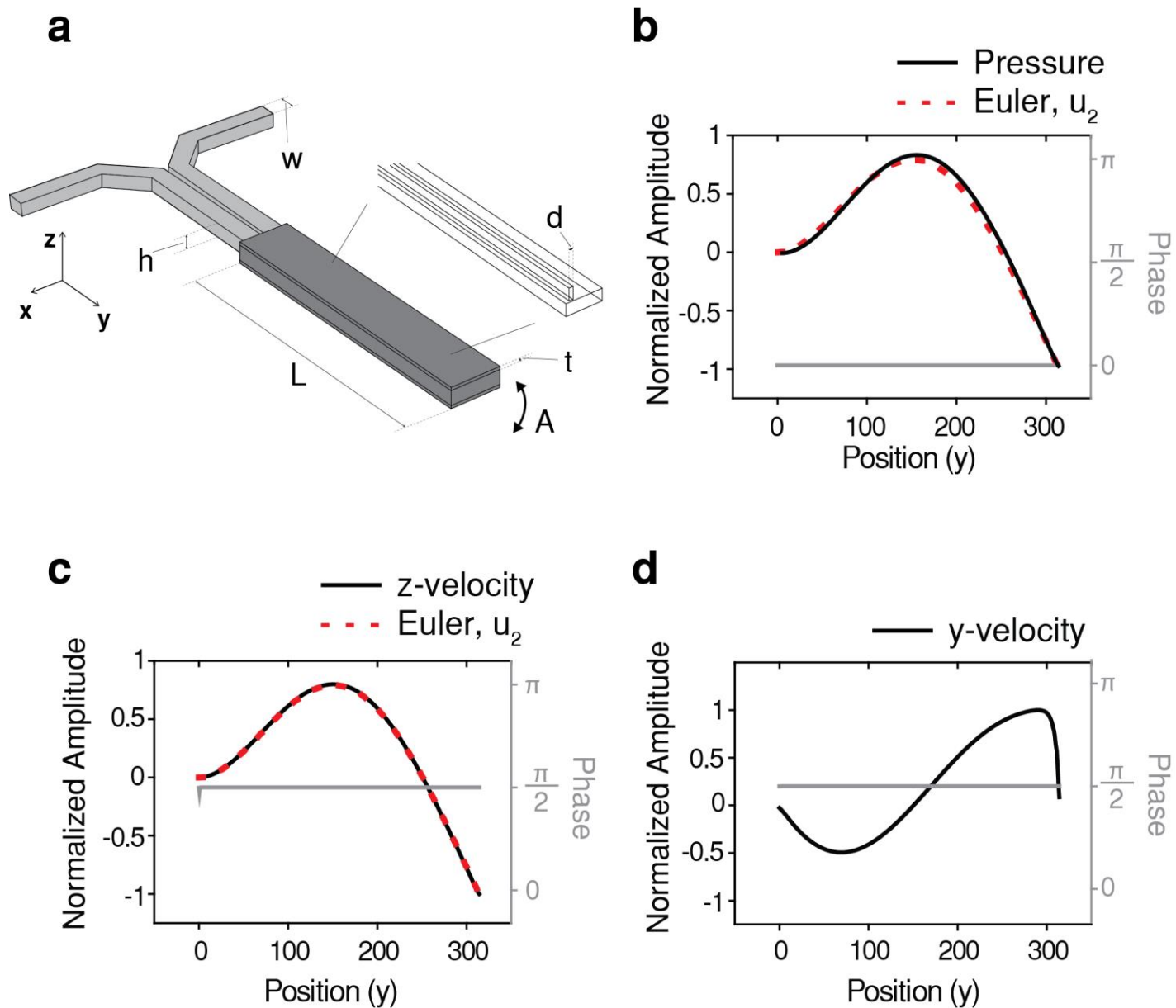


In the format provided by the authors and unedited.

Noninvasive monitoring of single-cell mechanics by acoustic scattering

Joon Ho Kang ^{1,2}, Teemu P. Miettinen ^{1,3}, Lynna Chen⁴, Selim Olcum ¹, Georgios Katsikis ¹,
Patrick S. Doyle^{1,5} and Scott R. Manalis ^{1,4,6*}

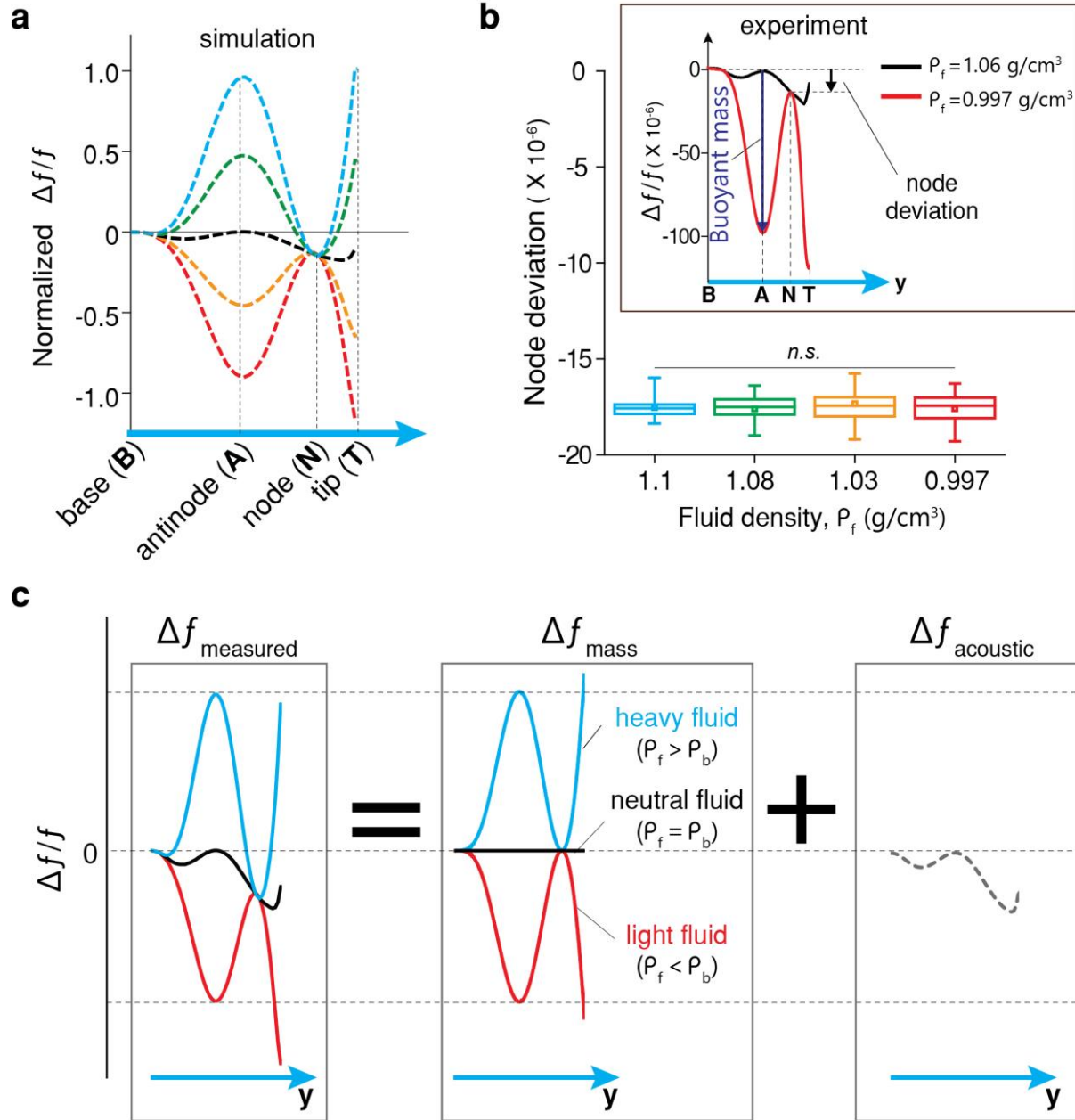
¹Koch Institute for Integrative Cancer Research, Massachusetts Institute of Technology, Cambridge, MA, USA. ²Department of Physics, Massachusetts Institute of Technology, Cambridge, MA, USA. ³MRC Laboratory for Molecular Cell Biology, University College London, London, UK. ⁴Department of Biological Engineering, Massachusetts Institute of Technology, Cambridge, MA, USA. ⁵Department of Chemical Engineering, Massachusetts Institute of Technology, Cambridge, MA, USA. ⁶Department of Mechanical Engineering, Massachusetts Institute of Technology, Cambridge, MA, USA.
*e-mail: srm@mit.edu



Supplementary Figure 1

SMR geometry and acoustic parameters from simulation.

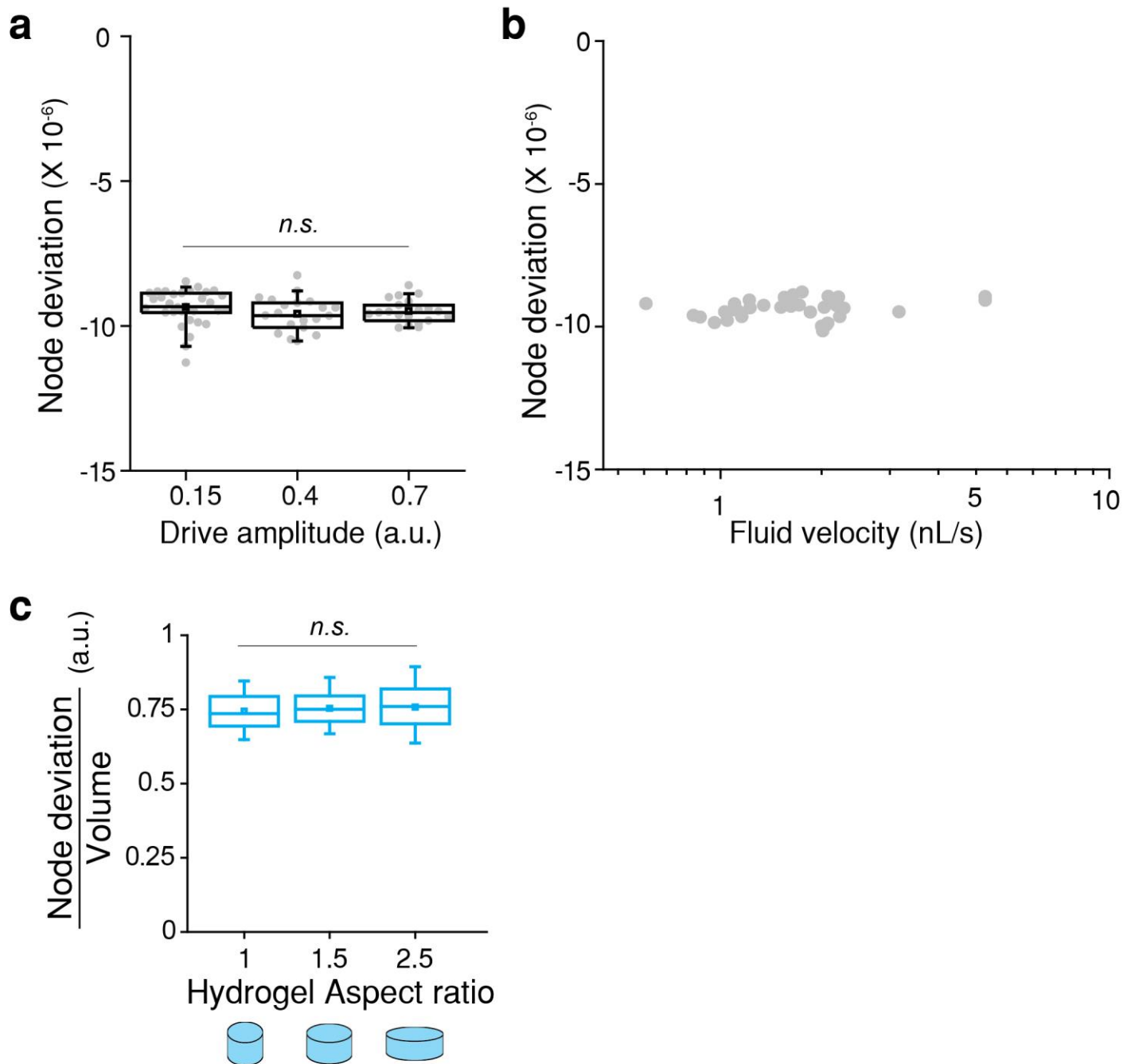
a, SMR geometry, dimensions (Supplementary Table 2) and coordinates. The fluid channel in the detection regime is covered with thin silicon layers (dark gray). Inset shows the buried channel. All dimensions are listed in Supplementary Table 2. **b–d**, Simulated acoustic pressure (**b**), z-velocity (**c**) and y-velocity (**d**). Amplitude (black) and phase (gray) are plotted along the top edge of the channel. The maximal amplitude of z-velocity and y-velocity were ~ 0.5 m/s and ~ 0.075 m/s, respectively. The second mode shape from the Euler–Bernoulli beam equation (u_2) is plotted as a red dashed line.



Supplementary Figure 2

Node deviation is independent of the mass change.

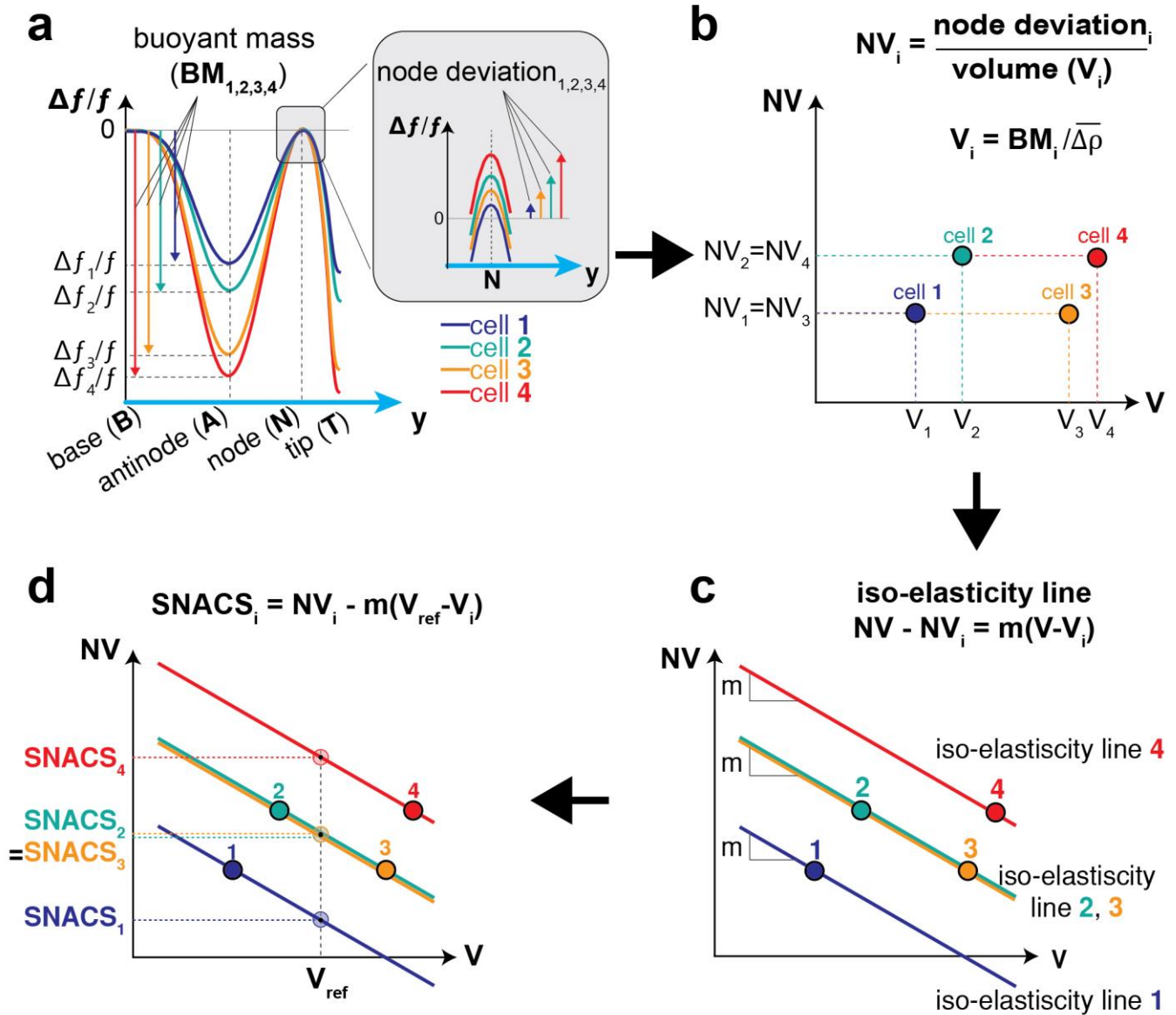
a, Frequency signals from simulations with 12- μm polystyrene bead ($\rho_b = 1.06 \text{ g/cm}^3$) immersed in fluids of different densities ($\rho_f = 1.1, 1.08, 1.06, 1.03$ and 0.997 g/cm^3 for blue, green, black, orange and red traces, respectively). Frequency signals were normalized relative to the result obtained for $\rho_f = 1.1 \text{ g/cm}^3$ (blue). **b**, Node deviation from experiments with 12- μm polystyrene bead immersed in fluids of the same densities as in **a** (1.1, 1.08, 1.03 and 0.997 g/cm^3 ; $n = 17, 97, 84$ and 120 beads, respectively, with the same colors as in **a**). Boxes indicate the interquartile range, squares represent means, whiskers extend to the 5th and 95th percentiles; $P = 0.32$ (one-way ANOVA). n.s., not significant. Inset: overlay of the frequency signal obtained from the density-matched fluid ($\rho_f = \rho_b = 1.06 \text{ g/cm}^3$, black) and water ($\rho_f = 0.997 \text{ g/cm}^3$, red). Buoyant mass (Δm , blue arrow) and node deviation (black arrow) are highlighted. **c**, Conceptual illustration of the frequency response, which is a superposition of the frequency response caused by both mass change, and the acoustic term independent of mass.



Supplementary Figure 3

Node deviation is not sensitive to SMR drive amplitude, particle flow velocity across the channel or particle shape.

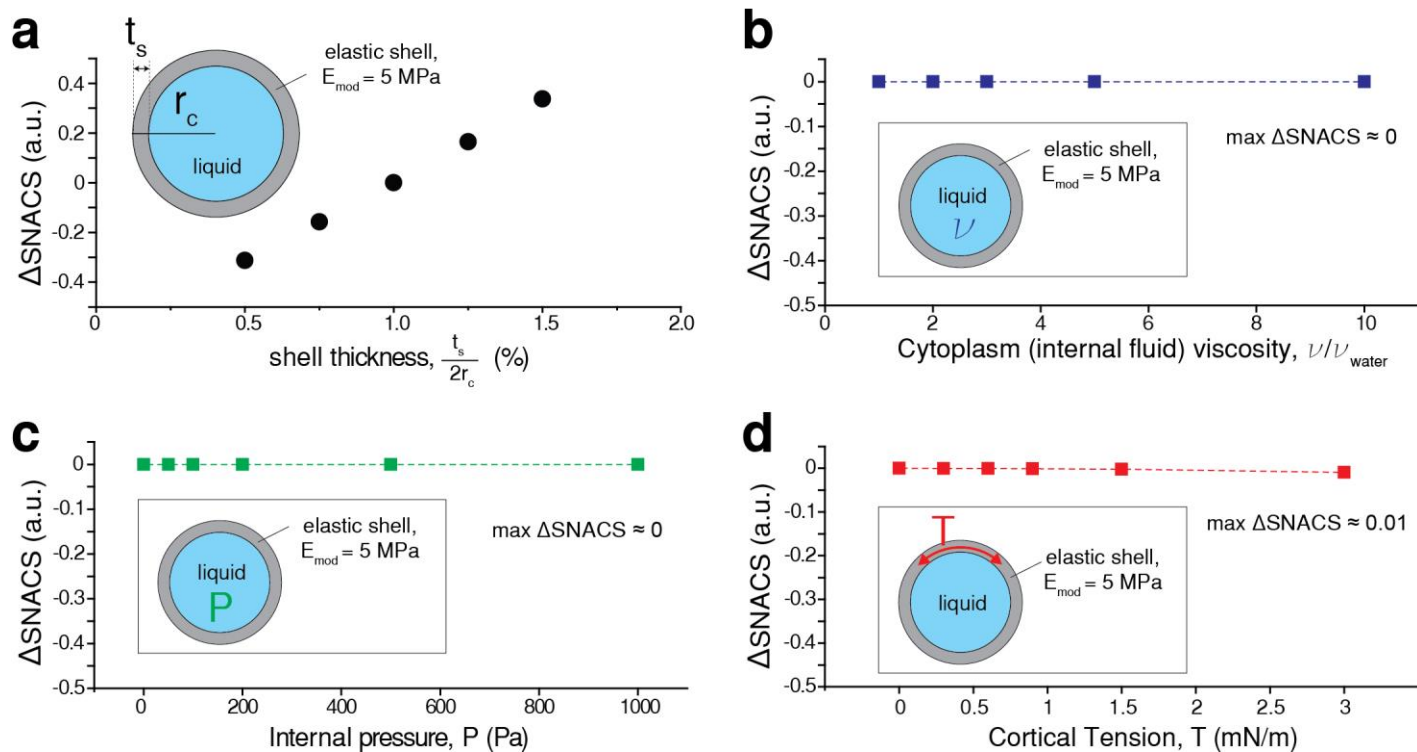
a, Node deviation from experiments with 10- μ m polystyrene beads measured by SMR vibrating in different amplitudes (0.15, 0.4 and 0.7; $n = 33, 21$ and 21 beads, respectively). $P = 0.37$ (one-way ANOVA). n.s., not significant. **b**, Node deviation from experiments with 10- μ m polystyrene beads measured by SMR with different fluid velocities ($n = 35$ beads). Velocities were derived from the transit time of the beads through the cantilever calculated from the duration of the resonant frequency shift of the beads. **c**, Node deviation versus aspect ratio (AR) from experiments with synthetic hydrogels of different shapes but the same volume (AR 1, 1.5 and 2.5; $n = 384, 423$ and 474 hydrogels, respectively). $P = 0.10$ (one-way ANOVA). n.s., not significant. In **a,c**, boxes indicate the interquartile range, squares represent means, and whiskers extend to the 5th and 95th percentiles.



Supplementary Figure 4

Illustration of the methodology used for obtaining the size-normalized acoustic scattering (SNACS) from the node deviation.

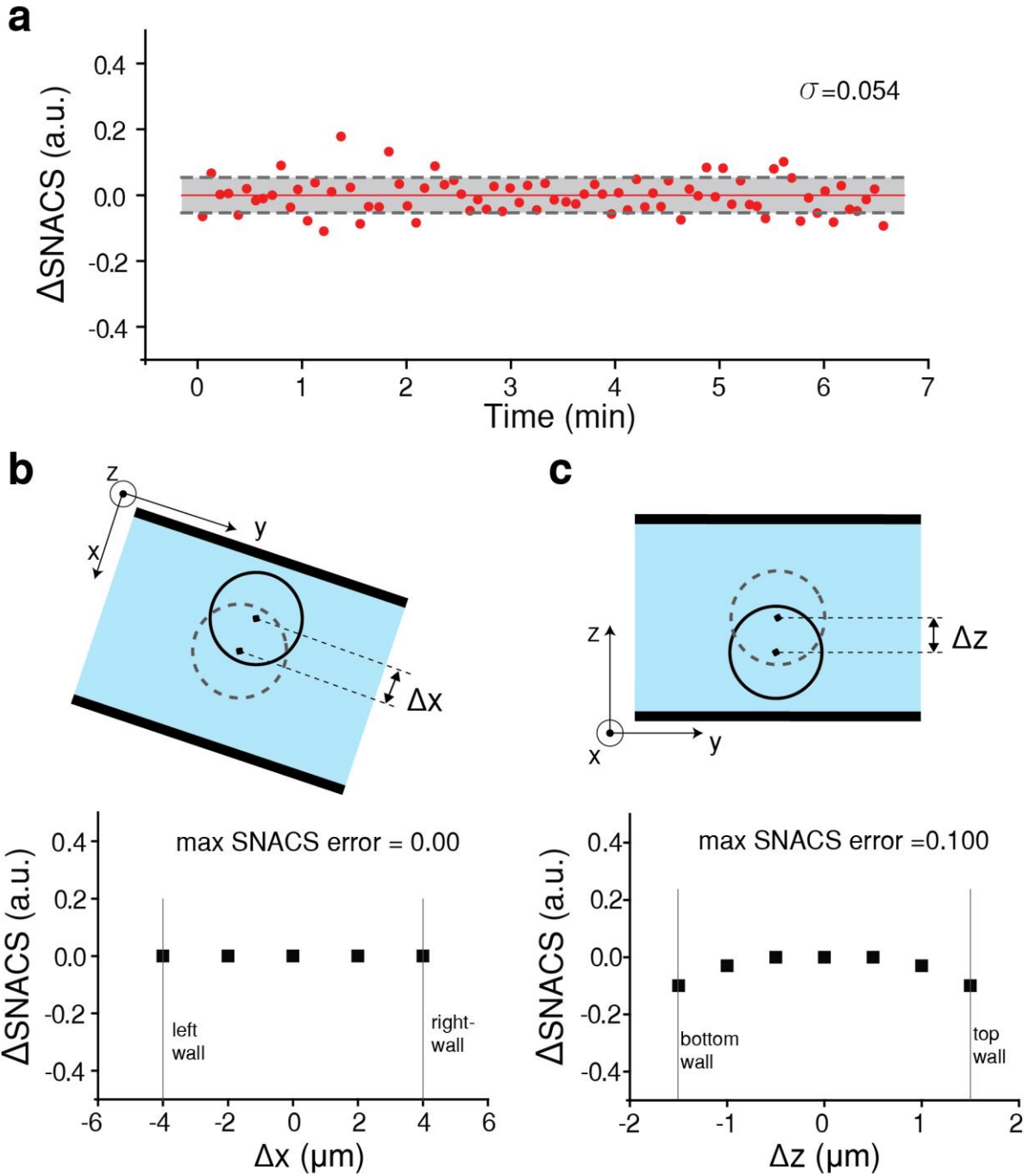
a,b, Steps for obtaining SNACS: The resonant frequency shifts ($\Delta f/f$) for each cell (1–4; colored curves) are used to measure the buoyant mass (BM) at the antinode and the node deviation at the node (**a**). Scatter plot of volume-normalized node deviation (NV) versus volume (V) (**b**). The volume of each cell ($V_{1,2,3,4}$) is obtained from the corresponding buoyant mass ($BM_{1,2,3,4}$) using the included equation. $\bar{\Delta\rho}$ is the median density of the population relative to the fluid. Data points of cells (1–4) are fit with isoelasticity lines (colored lines) with slope m (**c**). We obtained the slope (m) by performing a linear regression on the population data in the NV -versus- V scatter plot shown in Fig. 2b. The SNACS of each cell is obtained via the included equation (**d**). Graphically, the SNACS of each cell corresponds to an NV value at the intersection point between the isoelasticity line (colored lines) and the vertical line, $V = V_{ref}$ (black dotted line), where V_{ref} is set as the median volume of the population. See Methods for additional details.



Supplementary Figure 5

SNACS correlates with cortical thickness but is not sensitive to cytoplasmic viscosity, intracellular pressure or cortical tension based on FEM simulation using the cortical shell–liquid core model.

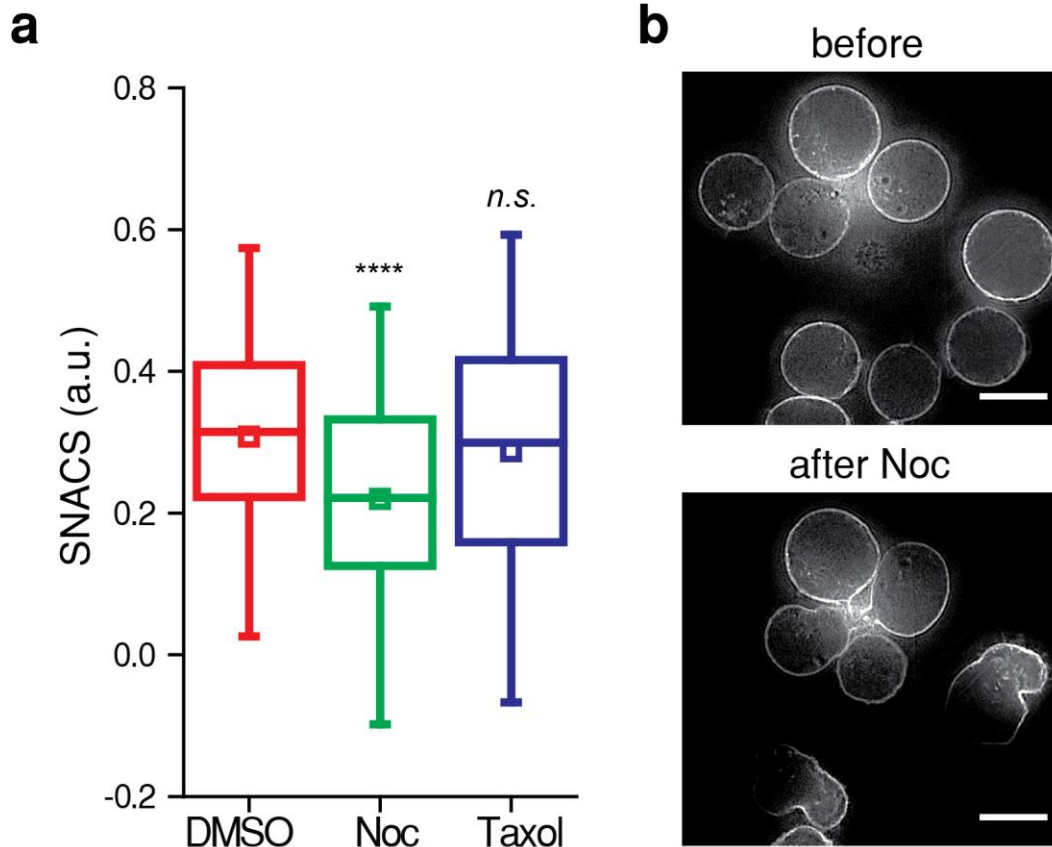
a–d, FEM simulation results of SNACS obtained from the cortical shell–liquid core model upon changes in cortical thickness (**a**), cytoplasm (internal fluid) viscosity (blue) (**b**), internal pressure (green) (**c**) and cortical tension (red) (**d**). SNACS changes relative to $t_s/2r_c = 1\%$, $\nu/\nu_{\text{water}} = 1$, $P = 0$, and $T = 0$ are plotted, respectively. We simulated tension by applying initial stress to the elastic shell region, in-plane direction. See Supplementary Note 2 for additional details. Insets: illustration of liquid-core elastic shell model with parameters being solved in FEM simulation. For all simulations, the total radius (r_c) and shell elastic modulus (E_{mod}) were fixed at $6 \mu\text{m}$ and 5 MPa , respectively.



Supplementary Figure 6

SNACS noise characterization.

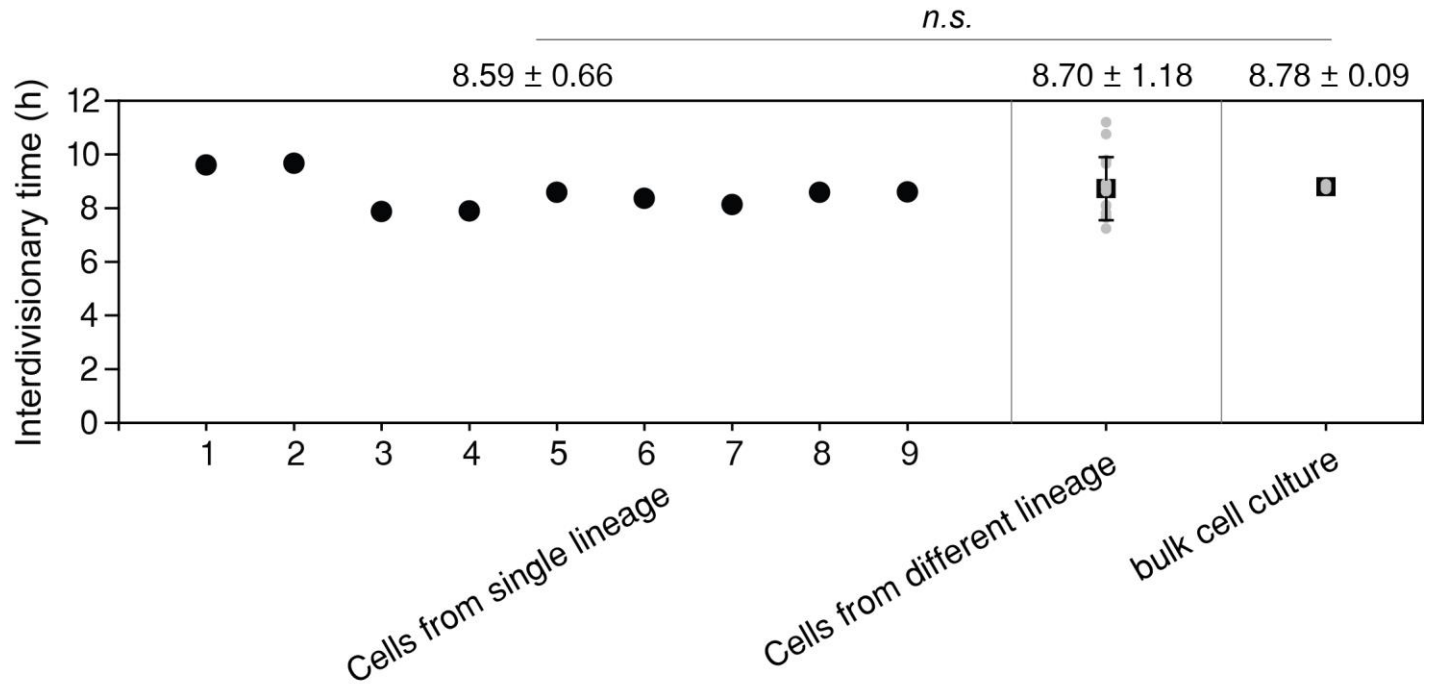
a, Continuous SNACS measurements of a single 12- μm polystyrene bead ($n = 79$ repeated measurements), implementing the same fluidic control strategy for continuous monitoring of single-cell SNACS (Fig. 3a). The mean (set to zero) is shown by the red line, and \pm s.d. (σ) is shown by the gray dashed lines. The gray area marks the data region within $\pm\sigma$. **b,c**, Illustration (top) and simulation results (bottom) of the cell model (Fig. 2a) with total radius (r_c) and shell elastic modulus (E_{mod}) of 6 μm and 5 MPa, respectively, with x-positional (**b**) and z-positional (**c**) offset from center of the channel. Vertical lines mark the offset distance from the center to positions where the outer surface of the cell touches channel walls.



Supplementary Figure 7

Microtubule perturbation affects actin cortex and SNACS.

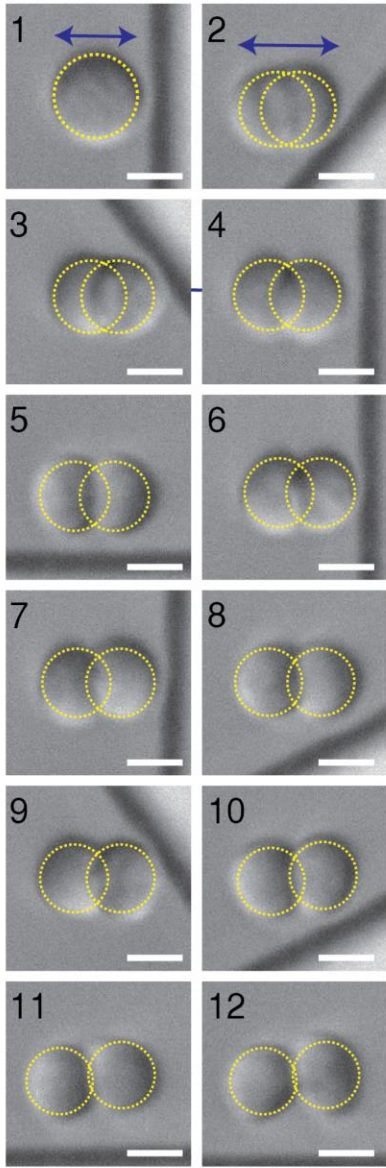
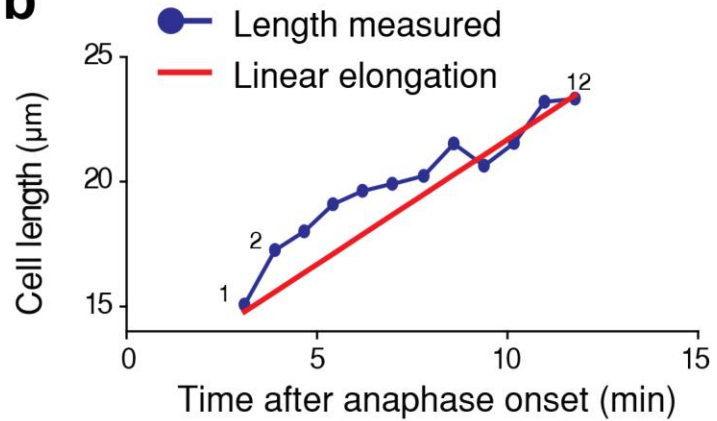
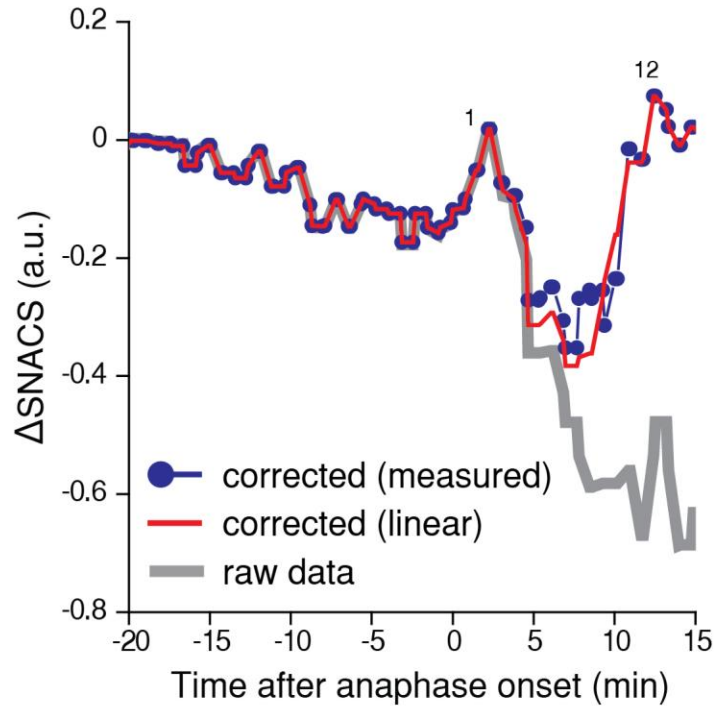
a, SNACS measured from L1210 cells treated with microtubule-affecting drugs: nocodazole (Noc, 1 $\mu\text{g/ml}$, $n = 760$ cells, $P = 2.8 \times 10^{-16}$) and Taxol (25 μM , $n = 511$ cells, $P = 0.12$). Statistical comparisons (two-sided Welch's t -test) were made to DMSO control (0.1%, $n = 718$ cells). Boxes indicate the interquartile range, squares represent means, and whiskers extend to the 5th and 95th percentiles; **** $P < 0.0001$; n.s., not significant. **b**, Representative images of actin cortex from live L1210 cells expressing LifeAct-RFP F-actin probe before (top) and after (bottom) treatment with nocodazole 1 $\mu\text{g/ml}$ ($n = 7$ fields of views). Scale bars, 10 μm .



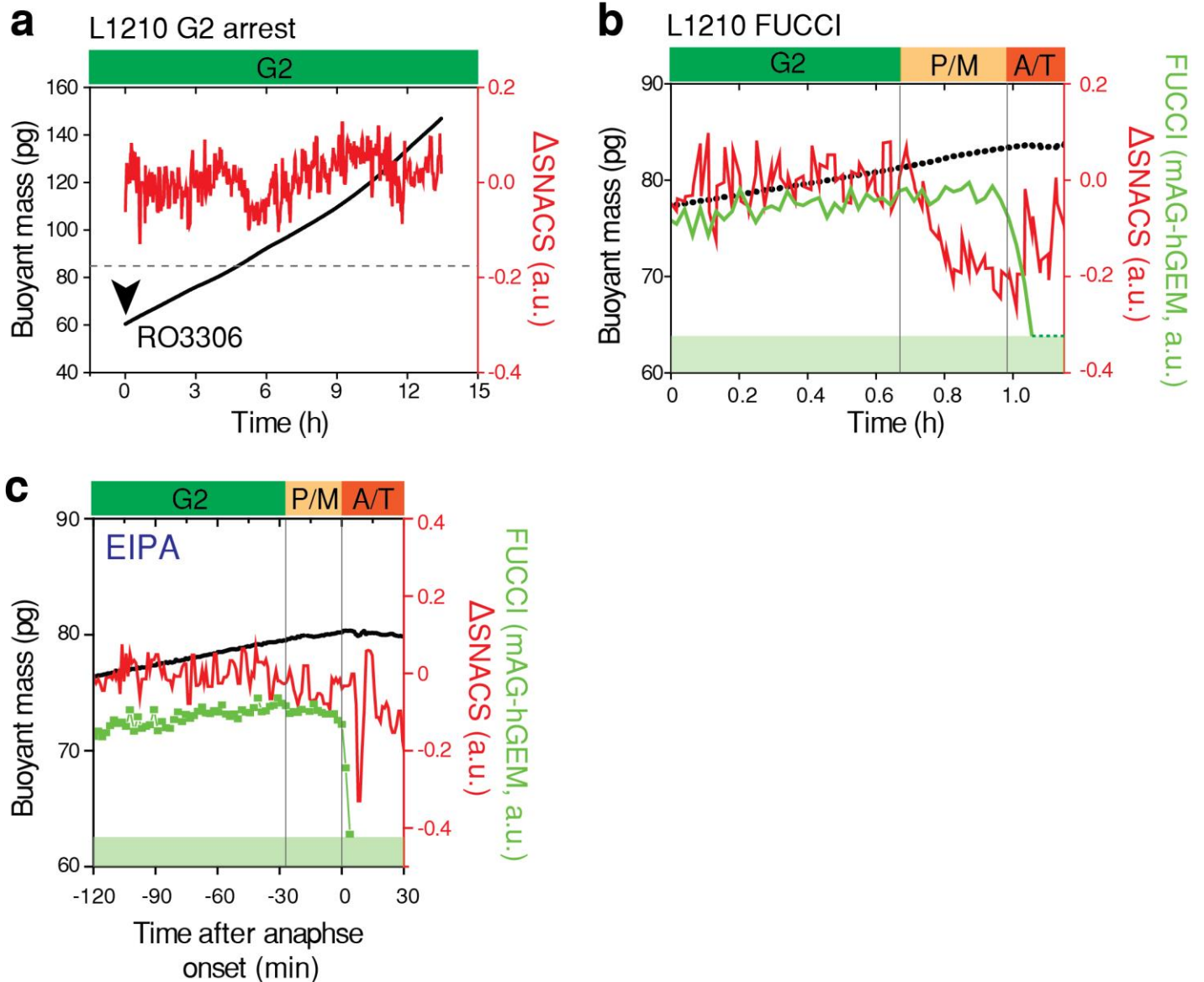
Supplementary Figure 8

Continuous SNACS measurements do not affect interdivision time.

Interdivision time (doubling time) of each daughter cell from the same lineage (left column, black dots), single cells from different lineages (middle column, gray dots) and from bulk cell culture (right column, gray dots). All single cells grown in SMR were exposed to the same conditions reported in the manuscript (SNACS measurement every 1 min). Higher temporal resolution can be achieved. However, repeating measurements more often than every 30 s may start to interfere with cell growth. For middle and right columns, data depict mean \pm s.d. Each mean \pm s.d. is listed on top. $P = 0.95$ (one-way ANOVA). n.s., not significant.

a**b****c****Supplementary Figure 9****Illustration of mass distribution correction in late mitosis.**

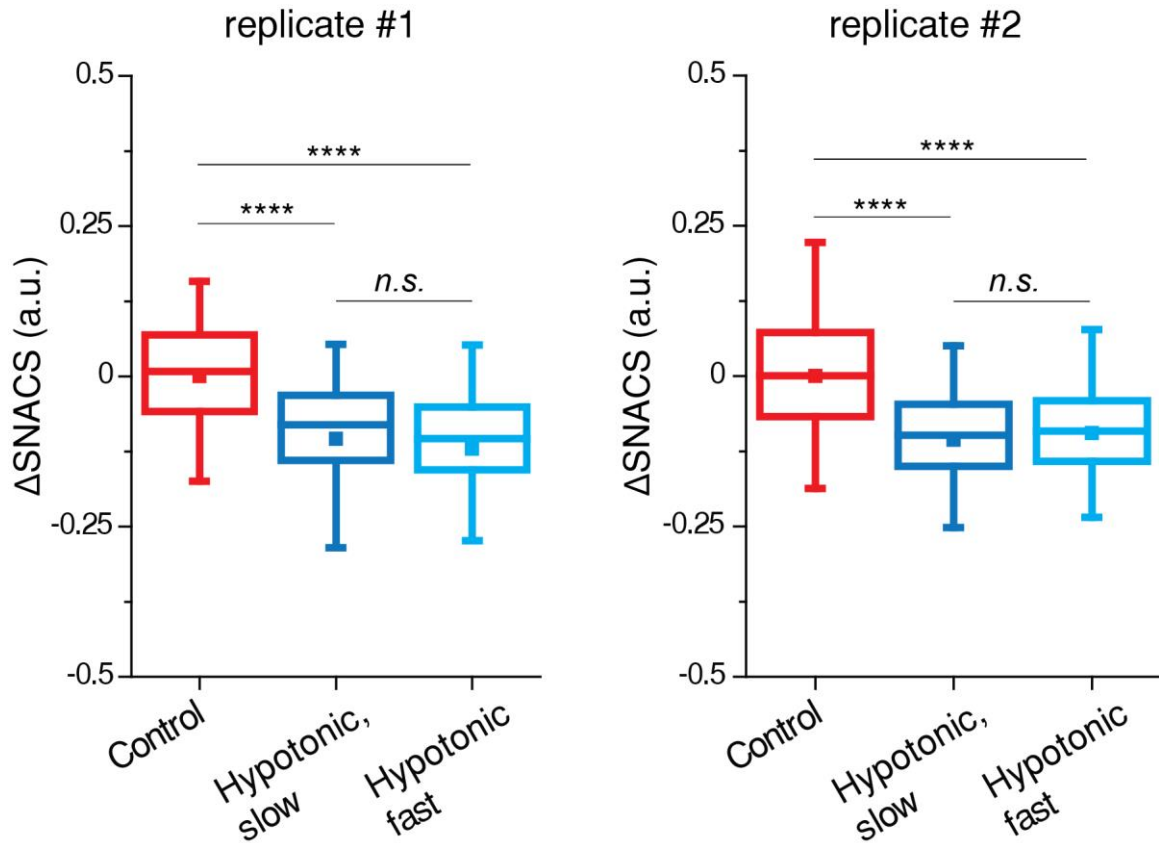
a, DIC images of the mitotic L1210 cell acquired on-chip, simultaneously with SNACS and buoyant mass measurement in late mitosis. For each time point, cells were fitted with overlapping spheres (yellow dotted lines) based on the measured elongation length (blue double arrows). Each number on the image marks the time progression. Scale bars, 10 μm . **b**, Cell length measured (blue dots) is plotted as a function of time after onset of anaphase. Numbers correspond to the images shown in **a**. The linear elongation derived from the first (1) and last image (12) is shown by the red line. **c**, SNACS before correction (gray), after correction for the mass elongation using length directly measured from DIC images (blue dots) and assuming linear elongation (red), plotted as a function of time after onset of anaphase. Numbers correspond to the images in **a**. See Supplementary Note 3 for additional details.



Supplementary Figure 10

SNACS change occurs in early mitosis and is reduced by EIPA treatment.

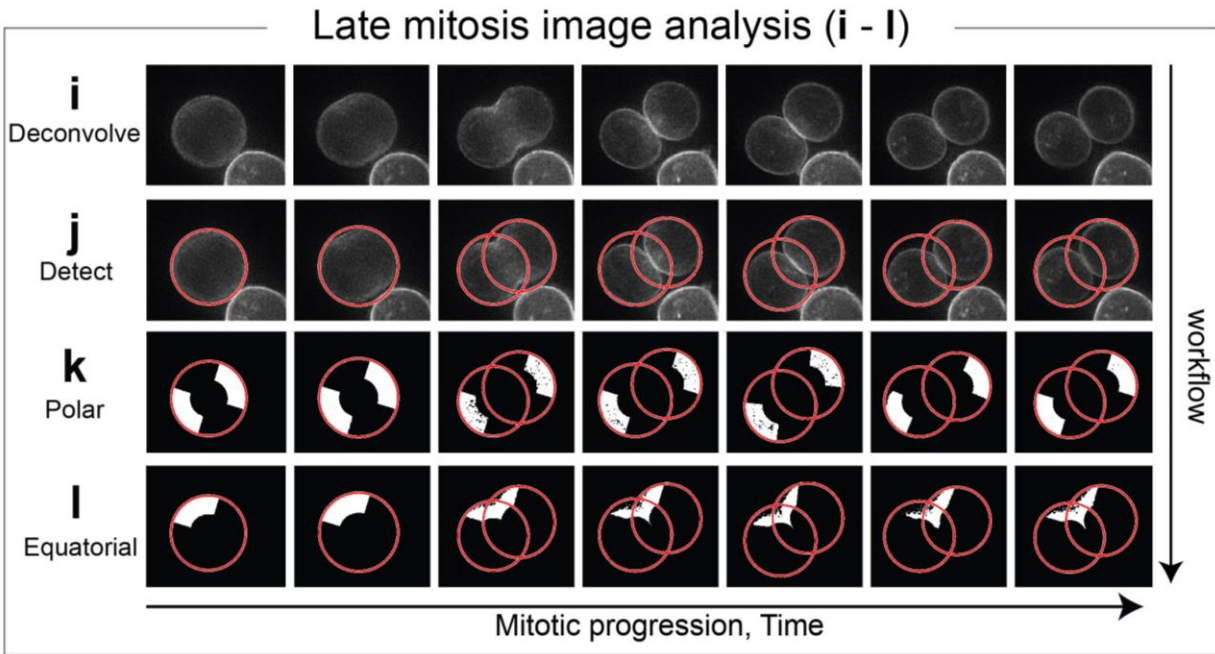
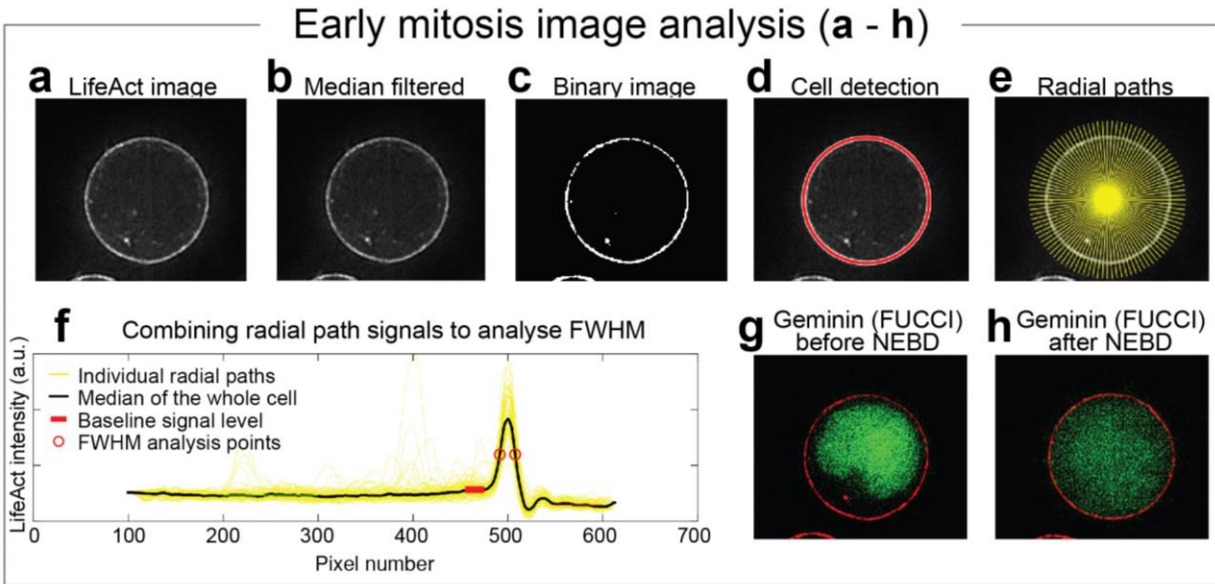
a, Buoyant mass (black) and SNACS (red) of L1210 treated with 2 μ M RO-3306, a CDK1 inhibitor. Arrowhead marks the start of drug exposure. The cell arrested in G2 continues to grow above the average size of L1210 cells at the mitotic entry (gray dashed line). **b,c**, Buoyant mass (black), SNACS (red) and FUCCI (green, mAG-hGem) of a control L1210 cell (**b**) and an L1210 cell treated with 10 μ M ethylisopropylamiloride (EIPA, an inhibitor of Na^+/H^+ antiporters) (**c**). The fluorescence detection limit of our system is shown by a green band at the bottom. An abrupt decrease in FUCCI (degradation of Geminin) marks the metaphase–anaphase transition. Vertical lines separate the cell cycle positions marked by color bars as shown in Fig. 3c. P, prophase; M, metaphase; A, anaphase; T, telophase.



Supplementary Figure 11

The rate of swelling does not affect SNACS change.

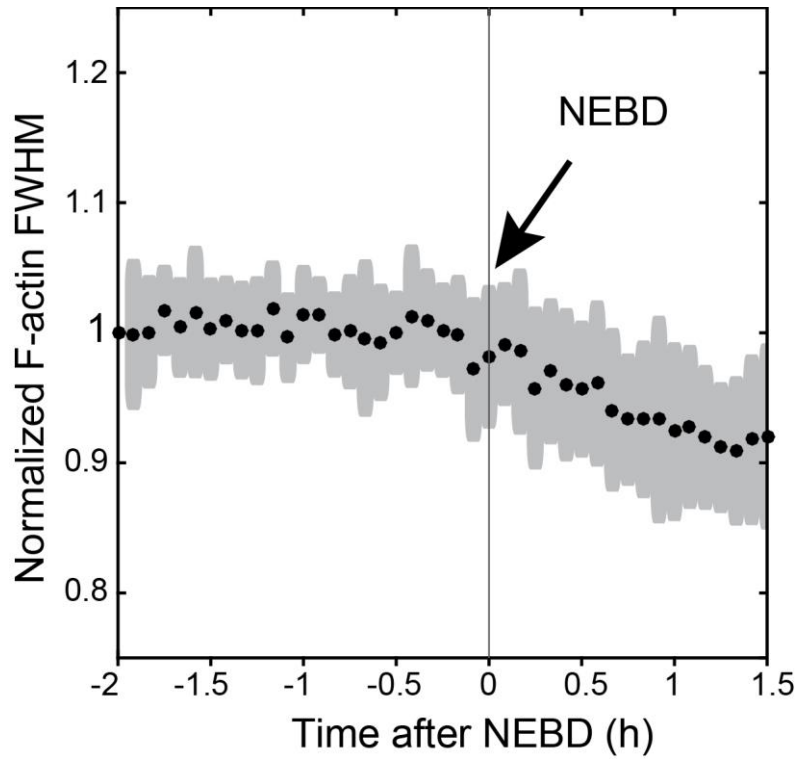
Results of two independent experiments showing SNACS change relative to controls (red; $n = 637$ and 566 cells for replicates 1 and 2, respectively) after hypotonic shocks that are slow (dark blue; $-\Delta 50$ mOsm over 20 min; $n = 558$ and 544 cells for replicates 1 and 2, respectively) or fast (light blue; $-\Delta 50$ mOsm instantaneous; $n = 507$ and 569 cells for replicates 1 and 2, respectively). Boxes indicate the interquartile range, squares represent means, and whiskers extend to the 5th and 95th percentiles; **** $P < 0.0001$; n.s., not significant. P (control versus hypotonic, slow) = 2.82×10^{-11} and 9.8×10^{-18} , P (control versus hypotonic, fast) = 6.63×10^{-14} and 5.1×10^{-15} , P (hypotonic, slow versus hypotonic, fast) = 0.32 and 0.36 for replicates 1 and 2, respectively. P values were obtained by one-way ANOVA, Fisher's least significant difference.



Supplementary Figure 12

Illustration of the image analysis.

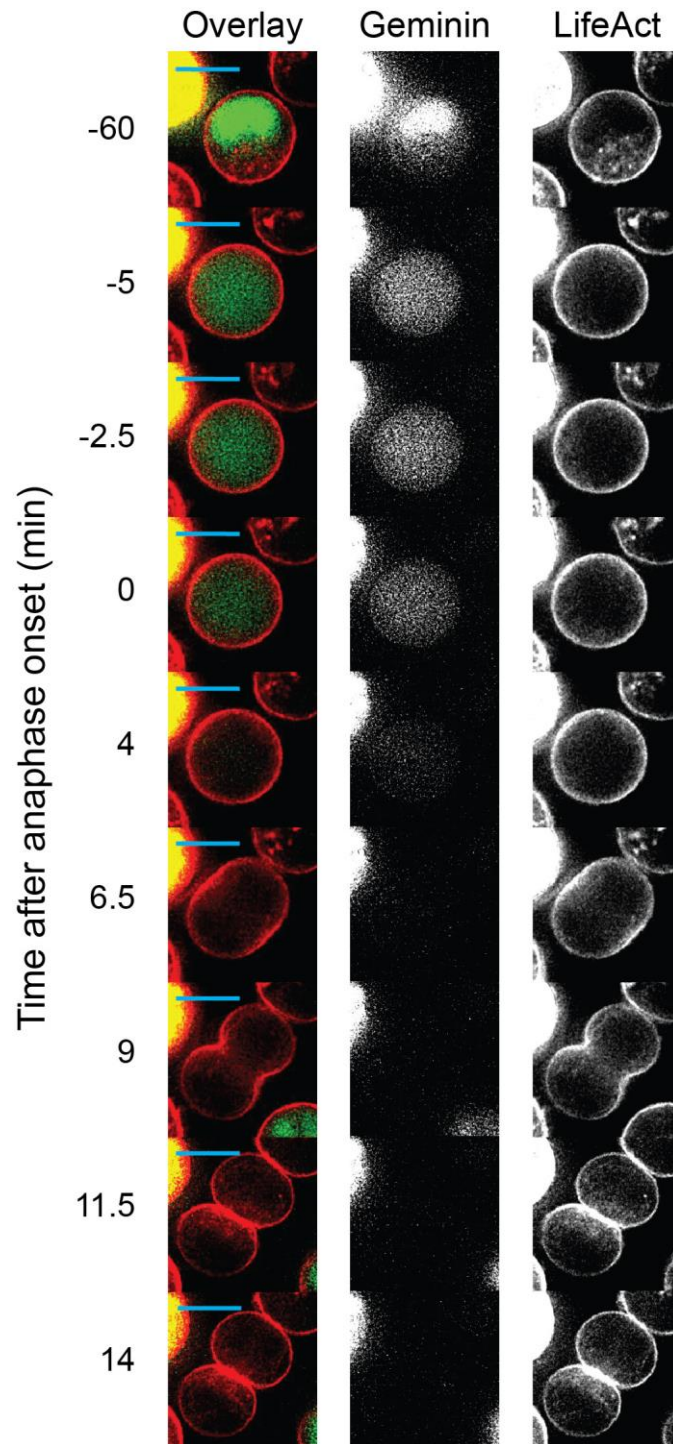
a-h, Successive steps of image analysis to obtain full width at half-maximum (FWHM) of F-actin cortex in early mitosis. Deconvolved image of the LifeAct signal from L1210 FUCCI cells expressing LifeAct-RFP F-actin probe (**a**). The image after application of the median filter (**b**). Binary converted image (**c**). Automatic detection of cell boundaries (red circle) (**d**). 100 radial paths (yellow lines) on which the LifeAct signal was quantified (**e**). Overlay of all radial path signals (yellow) as a function of distance from the cell center (**f**). The median of the radial paths (black line) was used to determine baseline within the cell, maximum signal at the actin cortex and, consequently, the FWHM. **g,h**, Nuclear envelope breakdown (NEBD) was used for aligning different cells to the same point in the cell cycle. NEBD was detected by the abrupt spread of the green Geminin fluorescence of the FUCCI from a restricted nuclear localization (**g**) to the whole cytoplasm (**h**). **i-l**, Successive steps of image analysis to detect equatorial and polar regions of the F-actin cortex in late mitosis. Steps in order (top to bottom) and from different time points (left to right): deconvolved image of an L1210 FUCCI cell expressing LifeAct-RFP F-actin probe (**i**). Detection of one or two cells in the image (red circles) (**j**). Assignment of the polar regions (white areas) (**k**). Assignment of the equatorial regions (white areas) (**l**). See Methods for additional details.



Supplementary Figure 13

F-actin cortical thickness decreases in early mitosis.

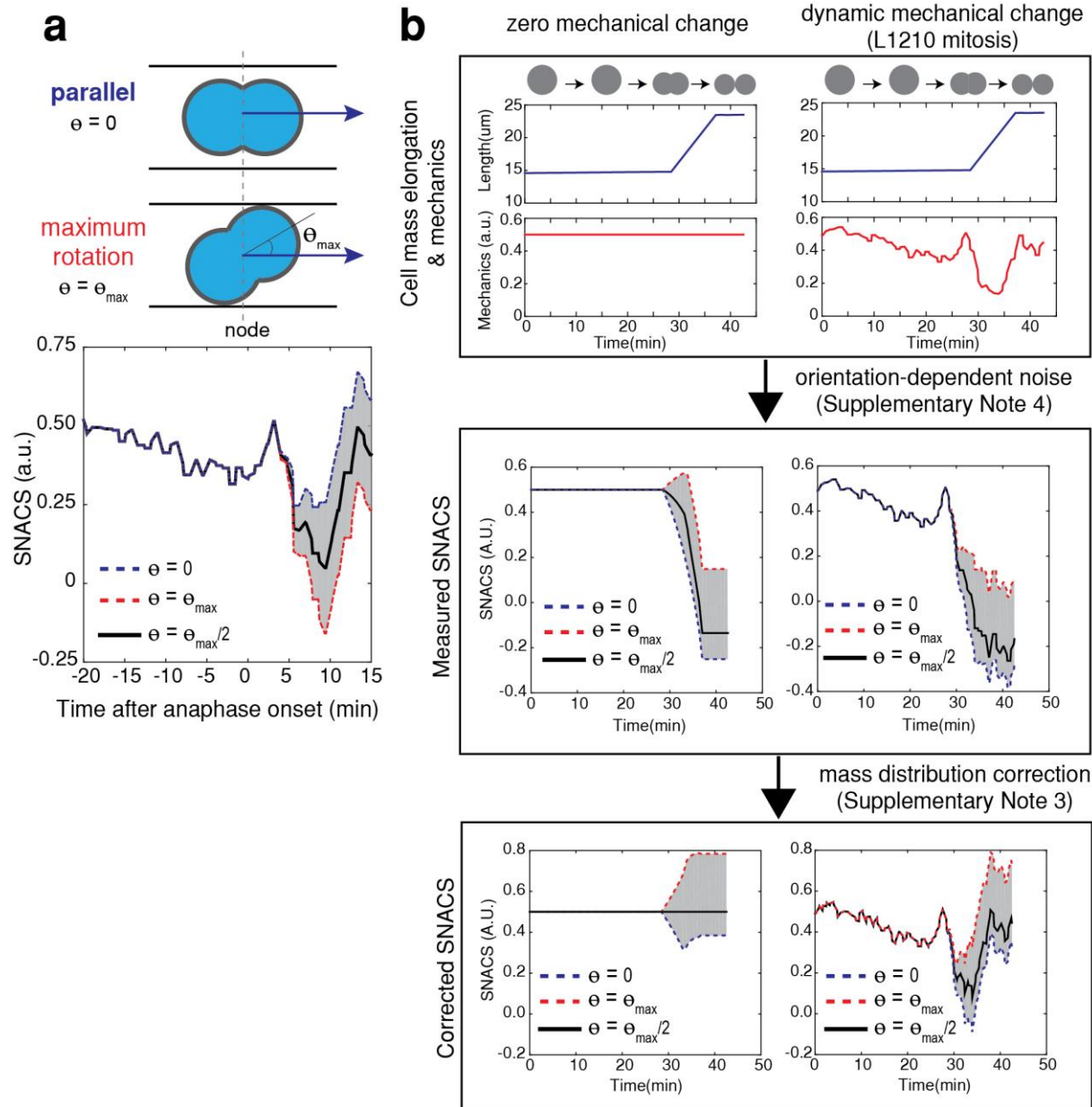
Mean FWHM (proxy of cortical thickness; black dots) and \pm s.d. (gray bars) of cortical LifeAct signal from L1210 Fucci cells expressing LifeAct-RFP F-actin probe in early mitosis ($n = 29$ cells). All FWHM signal was normalized to the time point at $t = -2$ h. Time 0 marks nuclear envelope breakdown (NEBD).



Supplementary Figure 14

Fluorescence images of F-actin and FUCCI in late mitosis.

Left column (Overlay), overlay of LifeAct (F-actin probe, red channel) and FUCCI (mAG-hGem, green channel) as a function of time after anaphase onset ($n = 7$ cells undergoing mitosis). Scale bars, 10 μm . Middle column (Geminin), fluorescence from the green channel only. Right column (LifeAct), fluorescence from the red channel only.



Supplementary Figure 15

Orientation-dependent noise and mass distribution correction during late mitosis.

a, Top, schematic showing the two extreme orientations of a cell during late mitosis: cells flowing parallel to the channel ($\theta = 0$) and maximally rotated ($\theta = \theta_{\max}$). Note that the dimension of the channel walls (black lines) and elongation length of a cell at a given time point determines the maximal rotation angle (θ_{\max}). Bottom, SNACS is corrected assuming three different orientations relative to the channel when cell is at the node: $\theta = 0$ (blue dash), $\theta = \theta_{\max}$ (red dash) and $\theta = \theta_{\max}/2$ (black solid). The gray area marks the orientation-dependent noise. See Supplementary Fig. 9 for raw SNACS. **b**, Effect of uncertainty in cell orientation on measured SNACS and corrected SNACS for two hypothetical cells both elongating as L1210 cells in mitosis (top panel, blue), but with different mechanical changes (top panel, red): zero change (left) and dynamic mechanical change similar to L1210 cells in mitosis (right). Two extreme orientations illustrated in **a** mark the boundary (blue and red dash) of orientation-dependent noise (gray area) in measured SNACS (middle panel). Corrected SNACS signals assuming an intermediate orientation ($\theta = \theta_{\max}/2$) during the entire time course are shown in the bottom panel. Representation of SNACS traces corresponding to each orientation are the same as in **a**. See Supplementary Note 4 for additional details.

Supplementary Table 1**List of energy terms.**

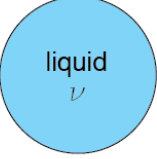

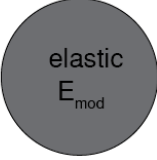
Parameter	Equation	Description
U_f	$\int_f \left[\frac{p_1^2}{2\rho c^2} \right] dV$	acoustic potential energy
T_f	$\int_f \left[\frac{1}{2} \rho v_1^2 \right] dV$	acoustic kinetic energy
$U_{p,s}$	$\int_{p,s} \left[\frac{1}{2} \sigma_{ij} \epsilon_{ij} \right]$	particle (shell) potential energy (elastic deformation)
$T_{p,s}$	$\int_{p,s} \left[\frac{1}{2} \rho x^2 \omega^2 \right]$	particle (shell) kinetic energy
U_c	$\int_c \left[\frac{p_1^2}{2\rho c^2} \right] dV$	liquid core acoustic potential energy (only applies to the cell model)
T_c	$\int_c \left[\frac{1}{2} \rho v_1^2 \right] dV$	liquid core acoustic kinetic energy (only applies to the cell model)

Supplementary Table 2**List of simulation parameters.**

Parameter	Values (units)	Description
w	20 (μm)	buried channel width
h	15 (μm)	buried channel height
L	315, 350 (μm)	cantilever (channel) length
t	2 (μm)	top, bottom silicon layer thickness
d	5 (μm)	fluid channel separation
A	1-100 (μm)	vibration amplitude
r_p	3 - 6 (μm)	particle radius
r_c	3 - 7 (μm)	total radius of a cell model
t_s	0.5 - 5(%)	thickness of the shell, relative to the radius
E_p	0.1 - 100 (MPa)	bulk Young's modulus of the particle
E_s	2-10 (MPa)	Young's modulus of the shell in liquid-core elastic-shell model
ρ_f	0.997 - 1.08 (g/cm^3)	fluid density
ρ_c	1.05 (g/cm^3)	cell density (both inner core and outer shell)
ρ_p	1.05 (g/cm^3)	bead density
ν_c	0.5	cell poisson's ratio (outer shell)
ν_p	0.34	bead poisson's ratio

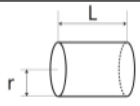

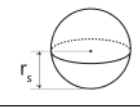
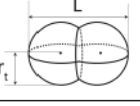
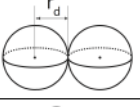
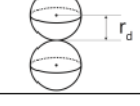
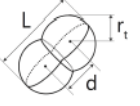
Supplementary Table 3

Different mechanical models.

Model	Model illustration	Simulation result
Viscous drop		cannot reproduce positive node deviation
Acoustic Impedance Mismatch		cannot reproduce positive node deviation
Bulk Elastic		can reproduce positive node deviation, but results in positive slope of isoelasticity line

Supplementary Table 4

Mass distribution function ($\lambda(x)$) for selected geometries and orientations.

Geometry	$\lambda(x)$	integration interval	Description (used)
	πr^2	$\left[-\frac{L}{2}, \frac{L}{2}\right]$	cylinder parallel (hydrogels)
	$2L\sqrt{r^2 - x^2}$	$[-r, r]$	cylinder perpendicular (hydrogels)
	$\pi(r_s^2 - x^2)$	$[-r_s, r_s]$	sphere (before anaphase)
	$\begin{cases} \pi(r_t^2 - (x + d/2)^2), & x < 0 \\ \pi(r_t^2 - (x - d/2)^2), & x > 0 \end{cases}$	$\left[-\frac{L}{2}, \frac{L}{2}\right]$	overlapping spheres (during anaphase transition)
	$\begin{cases} \pi(r_d^2 - (x + r_d)^2), & \text{if } x < 0 \\ \pi(r_d^2 - (x - r_d)^2), & \text{if } x > 0 \end{cases}$	$[-2r_d, 2r_d]$	doublet parallel (after anaphase transition)
	$2\pi(r_d^2 - x^2)$	$[-r_d, r_d]$	doublet perpendicular (after anaphase transition)
	$\begin{cases} \pi r_1^2, & \text{if } x < -q \\ \pi r_2^2, & \text{if } x > q \\ A(r_1, r_2, d/2 \sin \theta), & \text{else} \end{cases}$	$\left[-\frac{L}{2} \cos \theta, \frac{L}{2} \cos \theta\right]$	overlapping spheres rotated (during anaphase transition)

Note: $r_1 = \sqrt{r_t^2 - (x + q)^2}$, $r_2 = \sqrt{r_t^2 - (x - q)^2}$, $q = d/2 \cos \theta$

$A(r_1, r_2, d)$ refers to the area of overlapping circles of radius r_1 and r_2 , with their center separated by a distance of d

Supplementary Table 5**List of calculated cortical thickness change upon isometric volume expansion.**

swelling amount (% volume)	absolute cortex thickness change (%)	cortex thickness to diameter after swelling (%)	Note
0	0	1	
10	6.33	0.907	
14.1	8.65	0.874	plotted in Fig. 4d
15	9.14	0.867	
20	11.75	0.831	

Supplementary Note 1. Theory

1.1 Introduction

Using the Rayleigh Ritz Theorem, which equates time average kinetic energy and time averaged potential energy, resonant frequency of the Suspended microchannel resonator (SMR) containing a particle immersed in the fluidic channel can be obtained¹. It has been shown previously that a point-mass particle in the SMR of length L vibrating at its second mode shifts the resonant frequency as a function of particle position (y) along the cantilever²,

$$\left(\frac{\Delta f_2}{f_2}\right) = -1 + \left[1 + u_2^2(y/L) \frac{\Delta m}{m_{eff}}\right]^{-1/2} \approx -\frac{1}{2} u_2^2(y/L) \frac{\Delta m}{m_{eff}} \quad (1)$$
$$u_2(x) = \frac{1}{2} \left[(\cosh(\lambda_2 x) - \cos(\lambda_2 x)) - \left(\frac{\cosh(\lambda_2) + \cos(\lambda_2)}{\sinh(\lambda_2) + \sin(\lambda_2)} \right) (\sinh(\lambda_2 x) - \sin(\lambda_2 x)) \right]$$

where f is the resonant frequency of SMR vibrating at its second mode before the particle is introduced, u_2 is the normalized second mode shape, Δm is the mass change in the system upon loading the particle, m_{eff} is the effective mass of the unloaded cantilever, and λ_2 is the eigenvalue for the second mode ($\lambda_2 = 4.6941$). According to Eq. (1), the resonant frequency does not change when a particle is at the node (i.e., $\Delta f/f|_{node} = 0$ when $u_2(y) = 0$). However, we observe a non-zero frequency shift at the node (i.e. node deviation) from beads and cells (Fig. 1a).

In this note, we start our discussion with the theory that was developed to derive Eq. (1) and provide the assumptions that led to a discrepancy between theory (according to Eq. (1)) and measured node deviation (Fig. 1a). Next, we provide the details of the FEM simulation, which revealed new energy terms that were accounted for when calculating the resonant frequency change. Finally, we derive a new expression for the frequency response based on the FEM simulation results that successfully described node deviation measurements for both beads and cells (Figs. 1d,e and 2b).

1.2 Theory

We assume the vibration amplitude of the SMR follows the normalized second mode shape (u_2) from Euler-Bernoulli beam equation and is unchanged for sufficiently small mass loading ($\Delta m \ll m_{eff}$)¹

$$z(y, t) = Au_2\left(\frac{y}{L}\right) \cos(\omega t) \quad (2)$$
$$= Au(y) \cos(\omega t)$$

where A is the maximal amplitude and $\omega = 2\pi f$ for a SMR vibrating harmonically with frequency f . For this note, $u(y)$ refers to the normalized second mode shape. In the earlier theory, potential energy from the bending of the silicon layer surrounding the fluidic channel (Supplementary Fig. 1a) was considered to be the only term contributing to the total potential energy of the system, U_{total} . Therefore,

$$U_{total}(t) = U_{sil}(y, t) \quad (3)$$
$$= \int_0^l \frac{1}{2} EI \left(\frac{\partial z}{\partial y} \right)^2 dy$$
$$= \left[A^2 \int_0^l \frac{1}{2} EI \left(\frac{\partial u}{\partial y} \right)^2 dy \right] \cos^2(\omega t)$$
$$= U_{max} \cos^2(\omega t)$$

For the kinetic energy of the system, T_{total} , there are three contributing sources for kinetic energy (silicon layer, fluid, and particle) for which we provide

$$\begin{aligned}
T_{total}(y, t) &= T_{sil}(y, t) + T_f(y, t) + T_p(y, t) \\
&= \int_{sil} \frac{1}{2} \rho_{sil} \left(\frac{\partial z}{\partial t} \right)^2 dV + \int_f \frac{1}{2} \rho_f \left(\frac{\partial z}{\partial t} \right)^2 dV + \frac{1}{2} m_p \left(\frac{\partial z}{\partial t} \right)^2 \\
&= A^2 \left[\int_{sil} \frac{1}{2} \rho_{sil} \omega^2 u^2 dV + \int_f \frac{1}{2} \rho_f \omega^2 u^2 dV + \frac{1}{2} m_p \omega^2 u^2(y) \right] \sin^2(\omega t)
\end{aligned} \tag{4}$$

where m_p is the mass of the particle, ρ_{sil} and ρ_f are the densities of silicon layer and fluid, respectively. In the existing theory, the interaction between the fluid and particle is ignored and it is assumed that the particle and fluid have the same kinetics (i.e., $v(y) = \omega u(y)$). For this case, Eq. (4) simplifies to

$$\begin{aligned}
T_{total}(y, t) &= \frac{1}{2} A^2 \omega^2 [m_{eff} + (m_p - m_f) u^2(y)] \sin^2(\omega t) \\
&= T_{max}(y) \sin^2(\omega t)
\end{aligned} \tag{5}$$

where $m_{eff} = \frac{1}{2} \int \rho u^2 dV + \frac{1}{2} \int \rho_f u^2 dV$ when $y = 0$. Thus, using the Rayleigh-Ritz Theorem to equate the time-averaged potential energy $U_{max}/2$ with the time-averaged kinetic energy $T_{max}/2$ at $y=0$

$$U_{max} = T_{max} = \frac{1}{2} A^2 \omega_0^2 m_{eff} \tag{6}$$

where we set $\omega = \omega_0$ when $y=0$ (i.e., resonant frequency before particle enters the channel). We assume the potential energy of a system is not affected by the particle position and therefore constant ($U_{max} = C$). Then, applying Rayleigh-Ritz Theorem to equate $U_{max}/2$ and $T_{max}/2$ at non-zero and using Eq. (5),

$$\frac{1}{2} A^2 \omega_0^2 = \frac{1}{2} A^2 (\omega_0 + \Delta\omega)^2 (m_{eff} + \Delta m u^2(y)) \tag{7}$$

where $\Delta m = m_p - m_f$ and $\omega = \omega_0 + \Delta\omega$. This then simplifies to Eq. (1),

$$\left(1 + \frac{\Delta\omega}{\omega_0} \right)^{-2} = 1 + u^2(y) \frac{\Delta m}{m_{eff}} \tag{8}$$

So far, we have described how energy balance between kinetic and potential energy of the system collectively changes the resonant frequency of SMR. However, acoustic features in the SMR were ignored and several energy terms associated with acoustic fields in the SMR were neglected. First, we have assumed that the only term contributing to the potential energy is from the silicon layer. However, the potential energy stored in acoustic standing waves (Supplementary Fig. 1b and Supplementary Video 1) in the embedded microfluidic channel, as well as the energy stored in the elastic materials (particle and shell of the cell model) should also be included. Second, we have only considered velocities in the z-direction (i.e., normal to the surface of the cantilever, Supplementary Fig. 1c). We determined that the velocities along the cantilever (y-direction) could be as large as 10% that of the z-direction (Supplementary Fig. 1c, inset), and in the immediate vicinity of the node, the velocity in the y-direction is even greater than in the z-direction. Third, and most importantly, we have neglected the interaction between the particle and fluid environment by assuming the particle and nearby fluid have the same kinetics. However, as the particle scatters the acoustic field, it alters the kinetics of the neighboring fluid medium as well (Fig. 1c, inset and

Supplementary Video 2). By incorporating these three considerations into our FEM model, our simulation results match the experimental results (Fig. 1d,e and Supplementary Fig. 2).

1.3 Acoustofluidics

To develop a more general theory that includes the effect of the acoustic field, we begin with the governing equations for the fluids and their acoustic energies. Kinetics of a fluid is determined by its density ρ , pressure p , and individual fluid particle velocity v . These parameters are governed by the continuity equation for the mass and the Navier-Stokes equation³. Acoustic fields that result from a perturbation to these parameters can be written in terms of the zeroth, first, second, and third and higher-order terms as

$$\begin{aligned}\rho &= \rho_0 + \rho_1 + \rho_2 + \dots \\ p &= p_0 + p_1 + p_2 + \dots \\ \vec{v} &= \vec{v}_0 + \vec{v}_1 + \vec{v}_2 + \dots\end{aligned}\tag{9}$$

where the subscripts denotes the order of perturbation. 0th order represents the quiescent state and for simplicity we take $v_0 = 0$.

Taking only the 1st order perturbations into account and neglecting 2nd and higher order terms, the governing equations for fluids can be simplified into a wave equation

$$\nabla^2 p_1 = \frac{1}{c_0^2} \frac{\partial^2 p_1}{\partial t^2}\tag{10}$$

where c_0 is the speed of sound in the fluid, and $p_1 = c_0^2 \rho_1$. Assuming time-harmonic fields,

$$\begin{aligned}\rho_1(\vec{r}, t) &= \Re \{ \tilde{\rho}_1(\vec{r}) e^{-i\omega t} \} \\ p_1(\vec{r}, t) &= \Re \{ \tilde{p}_1(\vec{r}) e^{-i\omega t} \} \\ \vec{v}_1(\vec{r}, t) &= \Re \{ \tilde{\vec{v}}_1(\vec{r}) e^{-i\omega t} \}\end{aligned}\tag{11}$$

Eq. (10) reduces to a Helmholtz equation, given by

$$\nabla^2 p_1 - \frac{\omega^2}{c_0^2} p_1 = 0\tag{12}$$

It is worth noting that the harmonic vibration of the cantilever is the only necessary source for the acoustic perturbation. Since the equation governing the first order density ρ_1 , pressure p_1 and fluid velocity field v_1 is linear, all first order parameters will be proportional to A . Therefore, the kinetic and potential energy terms from the first-order acoustic fields,

$$\begin{aligned}w_v &= \frac{1}{2} \rho_0 v_1^2 \\ w_p &= \frac{1}{2} \frac{p_1^2}{\rho_0 c_0^2}\end{aligned}\tag{13}$$

will have $\sin^2(\omega t)$ or $\cos^2(\omega t)$ dependence as well as A^2 , similar to the energy terms shown in Supplementary Table 1. Therefore, when equating the total kinetic energy and potential energy (Rayleigh Ritz Theorem) to obtain the resonant frequency of the system, terms with A^2 effectively cancels out. In fact, we have experimentally seen that amplitude does not affect our node deviation signal (Supplementary Fig. 3). It is clear that since p_1 is in-phase with the cantilever vibration ($\propto \cos(\omega t)$, Supplementary Fig. 1b), $\omega_p \propto \cos^2(\omega t)$ and will therefore contribute to the

potential energy of the system, as expected. On the other hand, v_1 is out-of-phase with the cantilever movement ($\propto \sin(\omega t)$), Supplementary Fig. 1c,d), $\omega_v \propto \sin^2(\omega t)$ and will contribute to the total kinetic energy of the system. Next, we shift our discussion to the fluid-particle interaction, where a particle scatters the acoustic field around it, causing nearby fluid velocity and pressure to be

$$\begin{aligned}\vec{v}_1 &= \vec{v}_{in} + \vec{v}_{sc} \\ p_1 &= p_{in} + p_{sc}\end{aligned}\tag{14}$$

where \vec{v}_{in} and p_{in} are incident acoustic terms and \vec{v}_{sc} and p_{sc} are scattered terms. This will cause not only the acoustic fields to be scattered but the particle in the acoustic field to gain kinetic energy T_p and potential energy U_p related to the elastic deformation of the particle. Following the time-harmonic assumption, the gained kinetic energy can be obtained, as shown in Supplementary Table 1.

1.4 Revised theory incorporating acoustic effects

We incorporate all acoustic energy terms, including those resulting from fluid-particle interactions in to Eq. (3) and Eq. (4) in order to derive the resonant frequency change of the SMR.

$$\begin{aligned}U_{total} &= U_{sil} + U_f + U_p \\ T_{total} &= T_{sil} + T_f + T_p\end{aligned}\tag{15}$$

where U_f and U_p denotes acoustic potential energy and stored elastic energy of the particle, respectively. For sufficiently small changes in the frequency ($\Delta\omega \ll \omega_0$),

$$\begin{aligned}U_{total} &= U_0 + \Delta U(y) \\ T_{total} &= \alpha (\omega_0 + \Delta\omega)^2 + \Delta T(y)\end{aligned}\tag{16}$$

where U_0 and $T_0 = \alpha\omega_0^2$ are the time-averaged potential and kinetic energy of the system without the particle immersed in the SMR (i.e., $y=0$), respectively. $\Delta U(y)$ and $\Delta T(y)$ refer to change in potential and kinetic energy of fluids and particles, respectively, as a function of the particle position, y .

Applying the Rayleigh Ritz Theorem leads to:

$$\begin{aligned}\frac{\Delta\omega}{\omega_0} &= -1 + \left[1 - \frac{\Delta T(y) - \Delta U(y)}{U_0} \right]^{1/2} \\ &\simeq \frac{\Delta U(y) - \Delta T(y)}{2U_0}\end{aligned}\tag{17}$$

Eq. (17) generalizes the resonant frequency change of the system upon particle loading to be dependent on the total potential and kinetic energy of the system, unlike in Eq. (1), where frequency only depends on the particle position and mass. It is clear from Eq. (17) that even when a particle is located at the node with zero net out-of-plane motion, the disruption of the acoustic field would still result in a non-zero frequency shift.

The simulation results shown in Fig. 1d,e and Supplementary Fig. 2 was computed using the Eq. (17). This was accomplished by first numerically solving the Helmholtz equation (Eq. (12)) to obtain three fluid parameters (i.e., ρ , v , p), while varying the position of the particle along the channel. Then, we obtained the kinetic energy and potential energy of the system for each position (Supplementary Table 1), and subtracted the corresponding energy without the particle to get the term $\Delta U(y) - \Delta T(y)$. In Supplementary Note 2 we will discuss the necessary details of the simulation as well as provide more details for computing Eq. (17).

Supplementary Note 2. Simulation

When the acoustic domain of interest has non-trivial geometry with complicated boundary conditions, solving the governing equations analytically is challenging. Therefore we utilize Finite Element Method (FEM) simulations⁴ to solve the relevant equations provided in Supplementary Note 1. For FEM analysis, the governing equation (i.e., Wave equation: Eq. (10) for the time domain; Helmholtz equation: Eq. (12) for frequency domain) is to numerically solve for each individual 'block' within a mesh. In this note, we describe how the model is established and provide details on the post processing.

2.1 Geometry

For FEM analysis, COMSOL Multiphysics software 4.3 was used. The exact geometry of the SMR used for experiments in this work was reproduced in the software implementing the CAD design of SMR (Supplementary Fig. 1a and Supplementary Table 2). We embedded a particle in the detection regime of the cantilever (i.e., buried channel which is covered with thin silicon layers) and parameterized the y-position of the particle. We assumed the particle to be perfectly spherical, except where the effect of particle shape was tested. All dimensions used in the simulations are listed in Supplementary Table 2.

2.2 Model Setup

We used the 3-dimensional "Acoustic-Structure Interaction" module in the frequency domain provided by the software. The mathematical details of the governing equation and boundary conditions for the simulation are included in the manual⁴.

There are multiple possible sources that generate acoustic standing waves, but most of them will be second or higher order terms in the acoustic parameters (e.g., centrifugal force acting towards the tip and node). Here we neglect higher order acoustic sources and focus on the first order term, which is created by the out-of-plane motion of fluid channel in the cantilever, as given in Eq. (2).

$$a_t \equiv \ddot{z} = \omega^2 Au(y) a_b \equiv \ddot{z} = -\omega^2 Au(y) \quad (18)$$

where a_t and a_b are acceleration of the top and bottom surface, respectively. All simulations except viscous sphere model were performed under *pressure acoustics model* \rightarrow *fluid model* \rightarrow *linear elastic*. We used *sound hard boundary (wall)* condition for the fluid-channel boundary because of the high elastic modulus ($> 10^{11}$ Pa) and acoustic impedance of the silicon surrounding the fluid channel. We obtained the same results by using a boundary condition that accounts for the silicon elastic modulus (data not shown). We assumed the entire particle (and shell region for Cortical Shell – Liquid Core model) to be a *linearly elastic material* and *isotropic* solid. COMSOL then solves for the elastic solid-acoustic interaction, which incorporates the re-radiation of the acoustic field by the vibration of the solid interface driven by the incident pressure field. For the cell model, we treated the inner liquid core as a fluid with density $\rho = 1.05$ g/cm³ and sound velocity similar to salt water of the same density. We used the default *free tetrahedral* meshing for the entire geometries (Supplementary Table 2), except for the thin shell when performing simulation of the cell models, where we first meshed the outer surface with *free triangular* and used a sweep function towards the inner surface with *number of elements* set to 10. The mesh size of the *free triangular* and *free tetrahedral* mesh was set using the *general physics* option *extremely fine* and *fluid dynamics* option, *finer* respectively. Using these options, the minimal edge length of a typical element was set to 0.105 μ m for outer surface meshing of the particle and 0.285 μ m for the rest of the geometry. The position of the particle or cell in the y-direction was *parameterized* with steps of 5-10 μ m along the length of the cantilever to effectively capture the shape of the frequency response and enable the comparison with experimental data (Fig. 1d,e). The center of mass was positioned in the center of the channel for the all the simulations excluding the ones when we investigated how SNACS is affected by the positional offset from center of the channel (Supplementary Fig. 6).

2.3 Post Processing

Once COMSOL finished solving for the acoustic parameters as well as particle kinetics and elastic deformation, we integrated parameters (e.g. velocity, deformation) over specific geometries to obtain each energy term (Eq. (15)) as a function of the particle position (Supplementary Table 1). Once all energy terms were calculated as a function of the particle position, we then exported the data to MATLAB. To obtain $\Delta T(y)$ and $\Delta U(y)$, we subtracted all energy terms when the particle is at position $y = 0$, from the energy terms when the particles is at position y ;

$$\begin{aligned}\Delta U(y) &= (U_f(y) + U_{p,s}(y) + U_c(y)) - (U_f(0) + U_p(0) + U_c(0)) \\ \Delta T(y) &= (T_f(y) + T_{p,s}(y) + T_c(y)) - (T_f(0) + T_p(0) + T_c(0))\end{aligned}\quad (19)$$

where $U_{p,s}$ and $T_{p,s}$ denote the potential and kinetic energy, respectively, of the whole particle or the shell region of the cell model. The average deformation of the cell or particle was calculated assuming isometric expansion (i.e., $U_{p,s} = EA\Delta x^2/2x$, where E is elastic modulus, A is the surface area of the cell or particle and x is the length before deformation, Δx). U_c and T_c only apply to the cell model, where encapsulated inner core was treated as a fluid.

Lastly, to directly compare simulations with experiments, we converted the energy difference (in units of Joules, Eq. (19)) to a frequency shift (in units of Hz, Eq. (17)). To do this, we ran 10 μm polystyrene beads in both simulations and experiments and calibrated the energy difference ($\Delta U(y) - \Delta T(y)$) simulated when the bead is at the antinode ($y = y_{an}$) with the resonant frequency shift measured experimentally at the antinode ($\Delta f/f(y_{an})$).

2.4 Different mechanical models for cells

We also tested models other than the Cortical Shell – Liquid Core model, such as the Viscous Drop, the Acoustic Impedance Mismatch and the Bulk Elastic (Supplementary Table 3). For the Bulk Elastic model, the assumption of a uniform *linearly elastic material* was used. For Acoustic Impedance Mismatch, we assumed the cell to be a liquid sphere, with acoustic impedance set under the *Impedance* option. The Viscous Drop and Cortical Shell – Liquid Core model (Supplementary Fig. 5b) with the viscous core were simulated by selecting the *viscous fluid model* under *pressure acoustics model* while parameterizing the *dynamic* and *bulk viscosity* of the entire sphere or the fluid core of the Cortical Shell – Liquid Core. To simulate the effect of cytoplasmic pressure in our Cortical Shell – Liquid Core model (Supplementary Fig. 5c), we set the *pressure* under *initial values* to be parameterized within the range of 0-1000 Pa. The cortical tension model (Supplementary Fig. 5d) was developed similarly to previously reported COMSOL model⁵. Briefly, we applied a constant mechanical tension in the cortex by assigning an *initial stress* to the shell domain under *initial stress and strain*. Using Laplace's relationship, we assigned the *initial stress* in spherical coordinate (ρ, θ, φ ; relative to the center of the liquid core) as

$$\begin{bmatrix} 0 & 0 & 0 \\ 0 & pr_c/2t_s & 0 \\ 0 & 0 & pr_c/2t_s \end{bmatrix}\quad (20)$$

where p is the internal pressure, r_c is the cell radius, and t_s is the shell thickness.

Supplementary Note 3. Correcting mass distribution

3.1 Deconvolution of mass and acoustic signal

As we showed in the previous notes, the resonant frequency shift of the SMR at any point in time due to a particle present in the integrated channel is a superposition of the frequency change due to the added particles mass and acoustic scattering created by the particle (Supplementary Fig. 2),

$$\Delta f_{measured} = \Delta f_{mass} + \Delta f_{acoustic} \quad (21)$$

Here we assume Δf_{mass} is the frequency shift caused by a point-mass particle as shown in Eq. (1), which is proportional to the squared amplitude dependence of the mode shape, $u^2(y)$. However, a particle with a mass distribution along the cantilever would cause a frequency shift deviating from the squared mode shape. Therefore, in order to obtain the shape-insensitive acoustic term, $\Delta f_{acoustic}$, we need to correct for the mass distribution, Δf_{mass} , affecting $\Delta f_{measured}$. Here, we ignore the contribution of acoustic effects to the frequency shift and discuss only the contribution of the mass distribution to the resulting frequency shift. If a particle of length $2L$ with a linear mass distribution, $\lambda(x)$, is located at the position y along the cantilever, the shift in the resonant frequency is given by

$$\Delta f_{mass}(y) = \Delta f_{measured}(y_{an}) \frac{\int_{-L}^L \lambda(x)u^2(y+x)dx}{\int_{-L}^L \lambda(x)u^2(y_{an}+x)dx} \quad (22)$$

where y_{an} is the position of the antinode and $\Delta f_{measured}(y_{an})$ is the measured frequency shift at the antinode (i.e., buoyant mass). Although a point mass would create no mass-dependent frequency shift at the node ($y_n, u(y_n) = 0$), a particle with a non-zero size along the length of the cantilever will create a non-zero frequency shift when it is centered at the node. This contribution can be calculated from Eq. (22), and thus a correction can be made provided the size, shape and mass of the particle is known. The list of mass distributions, $\lambda(x)$, for some of the geometries that we encountered during this work is shown in Supplementary Table 4. For simplicity, we assumed the mass is homogeneously distributed around the geometry. As expected, compared to the single spherical particle, a doublet of particles will result in a larger frequency shift due to mass elongation. Although spheres have positional invariance making λ invariant to particle rotation, the λ for a doublet depends on its orientation relative to the cantilever (Supplementary Table 4).

3.2 Correction for cell elongation in anaphase

During the transition from a singlet to a doublet during anaphase, we assume that the total volume remains constant and that all geometries are the result of an overlap of two equally sized spheres (Supplementary Fig. 9). To accomplish this, we numerically solve for an individual sphere radius, r_t , with total elongation length, L , and volume, V , matching the following conditions:

$$\begin{aligned} L &= 4r_t - d \\ V &= 2 \int_{-r_t}^{r_t-y/2} \pi(r_t - x)^2 dx \end{aligned} \quad (23)$$

where d is the length of intersection between two identical spheres (Supplementary Table 4). With r_t obtained above, we add the following frequency shift to the node deviation we measured to correct for the mass elongation effect.

$$\Delta f_{correction}(y_n) = \Delta f_{measured}(y_{an}) \left[\frac{\int_{-L/2}^{L/2} \lambda_t(x)u^2(y_n+x)dx}{\int_{-L/2}^{L/2} \lambda_t(x)u^2(y_{an}+x)dx} - \frac{\int_{-r_s}^{r_s} \lambda_s(x)u^2(y_n+x)dx}{\int_{-r_s}^{r_s} \lambda_s(x)u^2(y_{an}+x)dx} \right] \quad (24)$$

where y_n is position of the node and λ_t and λ_s refer to the linear mass distribution of the overlapping spheres of individual radii of r_t and singlet of radius r_s , respectively (Supplementary Table 4). However, since λ_t depends on the exact orientation relative to the channel, there will be an error estimating the frequency shift, $\Delta f_{correction}$. For all data shown throughout this work, we assumed that the cells are oriented by an intermediate angle (i.e., $\theta_{max}/2$) during late mitosis (Supplementary Fig. 15). We further discuss the details of such orientation-dependent error in Supplementary Note 4.

Supplementary Note 4. Orientation-dependent noise

Orientation of a particle relative to the channel can affect mass distribution along the channel and result in a SNACS that is independent of the mechanical properties (Supplementary Note 3 and Supplementary Table 4). For example, the SNACS from a cylindrical particle flowing parallel through the channel at the node will be different from the case where the same particle has a perpendicular orientation (Supplementary Table 4, 1st and 2nd row, respectively). Thus, for non-spherical particles, the SNACS measurement contains an intrinsic noise that results from an uncertain orientation during detection at the node. For suspension cells, the shape is generally spherical up until late mitosis and so the orientation noise is negligible. This is evident by the low noise in our SNACS measurement during interphase (Fig. 3a,b).

For cells that deviate from a spherical shape, a spurious SNACS signal could arise if the cell gradually changes its orientation as it flows back-and-forth through the channel. There are two approaches for determining if a signal is spurious. The first applies to situations where the time range of a possible mechanical change is known (e.g. during mitosis). In this case, the SNACS signal can be measured from multiple cells. The resulting signals can be aligned and an analysis for statistical significance can be performed (for example Fig. 3c, where mitotic cells were aligned at the metaphase-anaphase transition). If a cell's orientation should gradually drift during a measurement, it will not be correlated across different cells.

The second approach applies to situations where changes in mechanics occur stochastically. In this case, the error resulting from orientation noise must be quantified. A threshold can then be established for determining if the SNACS measurement is revealing statistically significant changes in cell mechanics. The maximum orientation error in node deviation ($\Delta ND_{orientation}$) can be calculated provided the cell shape is known (e.g. by DIC imaging),

$$\Delta ND_{orientation} = \Delta f_{mass,or1}(y_n) - \Delta f_{mass,or2}(y_n) \quad (25)$$

where $\Delta f_{mass}(y_n)$ is given in Eq. (22). If the change in SNACS is sufficiently larger than the error obtained from Eq. (25), the resulting signal will be associated with changes in cell mechanics. We next present three examples to illustrate how orientation noise is estimated.

4.1 Cylindrical geometry

For a cylindrical particle of radius r and length L , the maximal node deviation change due to orientation error given by Eq. (25) is

$$\begin{aligned} \Delta ND_{orientation} &= \Delta f_{mass,c\parallel}(y_n) - \Delta f_{mass,c\perp}(y_n) \\ &= \Delta f_{measured}(y_{an}) \left[\frac{\int_{-L/2}^{L/2} \lambda_{c\parallel}(x) u^2(y_n + x) dx}{\int_{-L/2}^{L/2} \lambda_{c\parallel}(x) u^2(y_{an} + x) dx} - \frac{\int_{-r}^r \lambda_{c\perp}(x) u^2(y_n + x) dx}{\int_{-r}^r \lambda_{c\perp}(x) u^2(y_{an} + x) dx} \right] \quad (26) \end{aligned}$$

where, $\lambda_{c\parallel}, \lambda_{c\perp}$ is mass distribution function of a cylindrical sample lying parallel and perpendicular to the channel, respectively. From Eq. (26), a cylindrical hydrogel with a 10 μm diameter, 8 μm height and $\Delta f_{measured}(y_{an}) = 17 \text{ Hz}$, the resulting orientation noise is $\sim 0.004 \text{ Hz}$, which is equivalent to SNACS noise of ~ 0.006 (a.u.).

4.2 Cells in late mitosis

Here we estimate the orientation noise of a cell in late mitosis. Specifically, we use Eq. (25) to calculate the maximum error from orientation uncertainty as the cell elongates. Similar calculation done for the cylindrical hydrogel shown in Supplementary Note 4.1 will be performed. However, since the length of the elongated cell is greater than the channel width, the maximal rotation is now constrained. For example, overlapping spheres of total elongation length

L , and individual radius r_t flowing through the channel of width w can only rotate by an angle θ from y -axis (i.e. direction of a particle/fluid flow through the cantilever) (Fig. 1a and Supplementary Fig. 1a) which is given by,

$$2r_t + (L - 4r_t) \sin(\theta_{max}) = w \quad (27)$$

Using $w = 20 \mu m$ for our cantilever and the maximal angle provided from Eq. (27), Supplementary Fig. 15a bounds the maximum error due to orientation uncertainty as the cell elongates. Initially the error increases as the cell elongates. At a critical elongation length, the error reaches a maximum because the rotation within the channel begins to be constrained ($\theta_{max} < 90^\circ$).

4.3 Effect of sample orientation uncertainty on measured and corrected SNACS

In Supplementary Note 3, we described how to correct the SNACS signal for changes in mass distribution obtained by simultaneously measuring cell shape. Here, with the goal of showing the interplay between Supplementary Notes 3 and 4, we show the expected SNACS signal from a hypothetical cell that elongates during mitosis. In one case, we allow the mechanical properties to remain constant during elongation (Supplementary Fig. 15b, top panel, left), and for the other case, to change in a fashion similar to what we've observed in L1210 cells (Supplementary Fig. 15b, top panel, right). As shown in previous note (Eq. (22)), elongation causes the measured SNACS signal to be decreased due to mass distribution changes, but also variable depending on the orientation relative to the channel. The SNACS decrease and increased noise are independent from the cell's mechanical properties (Supplementary Fig. 15b, middle panel; gray area bounded by red and blue dashed line). In other words, SNACS measured at any given time point can fall along the gray region in Supplementary Fig. 15b middle panel. If we then apply the mass distribution correction scheme discussed in Supplementary Note 3 to the expected SNACS curves, we recover the trajectory where our error is determined by the upper and lower bound calculated from the orientation (Supplementary Fig. 15b, bottom panel; gray area bounded by red and blue dashed lines). It is clear that our orientation-dependent noise is small enough to distinguish cellular mechanical changes observed in mitotic L1210 cells (Supplementary Fig. 15b, right) from the hypothetical constant case (Supplementary Fig. 15b, left).

Supplementary Note 5. Swelling driven cortical expansion

Here we present the mathematics that govern the reduction of cortical thickness when the total volume expands. For this calculation, we assume that the volume expansion is isometric and that the cortical actin content and density does not change as a result of the expansion. Therefore, when a shell of thickness t_s , and total radius r_c (Figs. 2a and 4d) undergoes isometric volume expansion to bigger radius r'_c , the shell thickness would be reduced to t'_s ,

$$\frac{4}{3}\pi r_c^3 - \frac{4}{3}\pi(r_c - t_s)^3 = \frac{4}{3}\pi r'_c{}^3 - \frac{4}{3}\pi(r'_c - t'_s)^3 \quad (28)$$

Supplementary Table 5 lists some of the values that were calculated using Eq. (28).

Our FEM simulation revealed that increasing volume by 14.1% and, consequently, decreasing the cortex thickness to radius ratio by ~10% required an additional 10% decrease in cortical elastic modulus to match with the SNACS change we observe in early mitosis (Fig. 4c). This could be because cortical expansion during swelling causes actin cortex to be detached from the surface⁶ or because F-actins get partially damaged or ruptured by an increase in intracellular pressure⁷.

Supplementary References

- 1 Dohn, S., Svendsen, W., Boisen, A. & Hansen, O. Mass and position determination of attached particles on cantilever based mass sensors. *The Review of scientific instruments* **78**, 103303 (2007).
- 2 Lee, J., Bryan, A. K. & Manalis, S. R. High precision particle mass sensing using microchannel resonators in the second vibration mode. *Rev Sci Instrum* **82**, 023704 (2011).
- 3 Bruus, H. Acoustofluidics 1: Governing equations in microfluidics. *Lab Chip* **11**, 3742-3751 (2011).
- 4 "COMSOL Multiphysics Reference Manual, version 4.3", COMSOL, Inc, www.comsol.com.
- 5 Fischer-Friedrich, E. *et al.* Rheology of the Active Cell Cortex in Mitosis. *Biophysical journal* **111**, 589-600 (2016).
- 6 Steltenkamp, S., Rommel, C., Wegener, J. & Janshoff, A. Membrane stiffness of animal cells challenged by osmotic stress. *Small* **2**, 1016-1020 (2006).
- 7 Pritchard, S. & Guilak, F. The role of F-actin in hypo-osmotically induced cell volume change and calcium signaling in anulus fibrosus cells. *Ann Biomed Eng* **32**, 103-111 (2004).